




Model-based super-resolution reconstruction of T_2 maps

Wajiha Bano^{1,2}  | Gian Franco Piredda^{3,4,5}  | Mike Davies¹ | Ian Marshall² |
Mohammad Golbabaee⁶ | Reto Meuli⁵ | Tobias Kober^{3,4,5} | Jean-Philippe Thiran^{4,5} |
Tom Hilbert^{3,4,5} 

¹Institute for Digital Communications, University of Edinburgh, Edinburgh, United Kingdom

²Centre for Clinical Brain Sciences, University of Edinburgh, Edinburgh, United Kingdom

³Advanced Clinical Imaging Technology, Siemens Healthcare AG, Lausanne, Switzerland

⁴LTSS, École Polytechnique Fédérale de Lausanne, Lausanne, Switzerland

⁵Department of Radiology, University Hospital Lausanne (CHUV), Switzerland

⁶Computer Science Department, University of Bath, Bath, United Kingdom

Correspondence

Wajiha Bano, Institute for Digital Communications, University of Edinburgh, Alexander Graham Bell Building, King's Buildings, Thomas Bayer Road, Edinburgh, EH9 3FG, United Kingdom.
Email: wajiha.bano@ed.ac.uk

Funding information

The research leading to these results has received funding from the European Union's Seventh Framework Programme (FP7-PEOPLE-2013-ITN) under grant agreement n 607290 SpaRTaN and EPSRC Compressed Quantitative MRI grant, number EP/M019802/1.

Purpose: High-resolution isotropic T_2 mapping of the human brain with multi-echo spin-echo (MESE) acquisitions is challenging. When using a 2D sequence, the resolution is limited by the slice thickness. If used as a 3D acquisition, specific absorption rate limits are easily exceeded due to the high power deposition of nonselective refocusing pulses. A method to reconstruct 1-mm³ isotropic T_2 maps is proposed based on multiple 2D MESE acquisitions. Data were undersampled (10-fold) to compensate for the prolonged scan time stemming from the super-resolution acquisition.

Theory and Methods: The proposed method integrates a classical super-resolution with an iterative model-based approach to reconstruct quantitative maps from a set of undersampled low-resolution data. The method was tested on numerical and multi-purpose phantoms, and in vivo data. T_2 values were assessed with a region-of-interest analysis using a single-slice spin-echo and a fully sampled MESE acquisition in a phantom, and a MESE acquisition in healthy volunteers.

Results: Numerical simulations showed that the best trade-off between acceleration and number of low-resolution datasets is 10-fold acceleration with 4 acquisitions (acquisition time = 18 min). The proposed approach showed improved resolution over low-resolution images for both phantom and brain. Region-of-interest analysis of the phantom compartments revealed that at shorter T_2 , the proposed method was comparable with the fully sampled MESE. For the volunteer data, the T_2 values found in the brain structures were consistent across subjects (8.5–13.1 ms standard deviation).

Conclusion: The proposed method addresses the inherent limitations associated with high-resolution T_2 mapping and enables the reconstruction of 1 mm³ isotropic relaxation maps with a 10 times faster acquisition.

KEYWORDS

model-based reconstruction, parallel Imaging, super-resolution, T_2 mapping

This is an open access article under the terms of the Creative Commons Attribution License, which permits use, distribution and reproduction in any medium, provided the original work is properly cited.

© 2019 The Authors. *Magnetic Resonance in Medicine* published by Wiley Periodicals, Inc. on behalf of International Society for Magnetic Resonance in Medicine

1 | INTRODUCTION

Spin-spin relaxation characterized by its relaxation time T_2 is 1 of the 2 principal relaxation mechanisms in MRI. Its quantification, typically referred to as T_2 mapping, provides important information about the tissue of interest. Previous studies have demonstrated the importance of T_2 mapping to study various neurological conditions such as stroke,¹ epilepsy,² multiple sclerosis,³ and tumor detection.⁴

Conventionally, T_2 is measured by sequentially acquiring several spin-echo (SE) images, each with a different echo time (TE) and subsequently fitting a mono-exponential decay. This is commonly acknowledged as a gold standard, despite residual diffusion effects affecting the T_2 quantification. Nonetheless, the long acquisition times (TAs) of around 50 min for whole-brain coverage in 2D is impractical for clinical applications. As an alternative approach, the multiple-echo SE (MESE) sequence in the Carr-Purcell-Meiboom-Gill condition⁵ uses subsequent refocusing pulses to acquire multiple echoes for each excitation, reducing the total acquisition length. However, the quantitative accuracy of the sequence is compromised by imperfect refocusing. The imperfect refocusing results in the formation of stimulated (secondary) echoes that disrupt the T_2 decay of the primary SEs.⁶ The effect of the stimulated echoes can be reduced by ignoring the first echo (because this pure SE biases the fitting of the subsequent stimulated-echo-contaminated data) while fitting the relaxation curve.⁷ However, it has been shown that skipping echo approaches still yield highly variable results with errors that depend on flip angle, T_2 , and echo train length.⁸ Therefore, more complex signal models are required to accurately estimate T_2 .⁶

The ability to accurately and precisely map T_2 at high resolution (e.g., 1-mm³ isotropic voxel size) in large volumes may help to improve the quantification of small focal changes such as multiple sclerosis lesions or brain areas causing focal seizure onset in epilepsy. However, using thin slices in a 2D MESE acquisition is challenging due to the reduced signal-to-noise ratio (SNR) and increasing difficulties to achieve a good slice profile. Furthermore, radio-frequency pulses with long duration are required to excite thin slices leading to longer echo spacings (ΔTE).⁹ The increased ΔTE s aggravate and inhibit an accurate quantification of short T_2 values. In addition, true T_2 -weighting is difficult to obtain in reasonable TAs with 3D acquisition methods because a long repetition time (TR) is required to fully recover the magnetization to equilibrium between excitations. Because all spins in the field of view (FOV) of a 3D acquisition are excited by every pulse, the recovery time cannot be used for interleaved slice sampling, rendering the sequence less efficient.¹⁰ Furthermore, a 3D acquisition is also limited by specific absorption rate safety constraints. A large amount of power is deposited if multiple nonselective 180° pulses are used which can easily exceed the specific absorption rate limits.¹¹

A fundamental consideration in any MRI experiment is to optimally balance image resolution, SNR, and TA. Various methods have been published to accelerate quantitative mapping methods, for example applying model-based reconstructions,^{7,12-14} low-rank approaches,^{15,16} or sparsity constraints^{17,18} to highly undersampled acquisitions. However, these methods experience a low SNR and use low spatial resolution to counteract this effect. On the other hand, it has been shown that super-resolution (SR) reconstruction provides a better trade-off between TA, spatial resolution, and SNR.^{9,10} The earlier SR methods^{19,20} focused on the improvement of the in-plane resolution of MR images. To achieve this in-plane resolution improvement, several images with a subpixel shifted FOV in the in-plane directions were acquired. However, the subpixel shift of the FOV in the in-plane directions correspond to a linear phase modulation in the k-space and does not acquire new frequency information.²¹ Thus, the apparent improvement in the in-plane resolution in this case is due to an improvement in the SNR.

Later, most SR methods focused on decreasing the slice thickness and reaching voxel isotropy by exploiting the aliasing as a result of downsampling in the slice-select direction.²² The resolution is thereby enhanced by acquiring multiple low-resolution images with a shift of the FOV in the slice direction,¹⁰ 3 orthogonal slice orientations²² or rotated slice orientations,²³ and subsequently combining the images by solving a nonlinear inverse problem. In quantitative MRI, SR reconstruction benefits from combining the parametric model with the SR model. This has been shown in T_1 mapping²⁴ where the relaxation model was combined with the SR model allowing the direct estimation of a high-resolution T_1 map from low-resolution images. However, the acquisition of multiple low-resolution images results in long scan times (TA > 20 min), hence limiting its use for clinical applications.

Both the SR and model-based reconstructions are based on solving an inverse problem using iterative optimization methods. The present work investigates the combination of SR and model-based reconstruction to exploit the respective advantages (i.e., high-resolution and fast TA) in the application of quantitative T_2 mapping. The proposed method is based on multiple 2D MESE acquisitions, which were highly undersampled to compensate for prolonged scan time. The method was tested on a phantom and 4 healthy volunteers. An early version of this framework was presented at the Annual Meeting & Exhibition of the ISMRM in 2017.²⁵

2 | THEORY

SR reconstruction is a method to obtain a high-resolution image from a series of low-resolution images, where each low-resolution has a different FOV or orientation. Each FOV or orientation can be expressed as a different

geometric transform T_j (with $j = 1, \dots, J$, and J the number of transformations) from the high-resolution image to the low-resolution image. The resolution is enhanced because the different FOVs or orientations contain complementary information. The reconstructed high-resolution image on the other hand benefits from the high SNR of the low-resolution images, which are typically acquired with a high in-plane resolution and a low through-plane resolution, i.e., thick slices.

Let \mathbf{x}_n (with $n = 1, \dots, N$, and N the number of SEs) represent a high-resolution T_2 -weighted series of vectorized images and $\mathbf{y}_{j,n,c}$ (with $c = 1, \dots, C$, and C the number of coils) be the undersampled low-resolution k-space measurements acquired with a MESE sequence. The acquisition of the undersampled low-resolution $\mathbf{y}_{j,n,c}$, can be modeled by:

$$\mathbf{y}_{j,n,c} = PF \{ S_{j,c} \downarrow T_j \mathbf{x}_n \} + \boldsymbol{\eta}_{j,n,c} \quad (1)$$

where T_j is the geometric transformation representing a rotation or translation of the FOV (Figure 1), \downarrow is a downsampling operator that maps the high-resolution grid to the low-resolution grid, $S_{j,c}$ are the complex coil sensitivities calculated separately for each transformation, F is the forward discrete Fourier operator, and P is a binary undersampling mask. According to Gudbjartsson and Patz,²⁶ the noise $\boldsymbol{\eta}_{j,n,c}$ in MRI can be assumed to be additive, white, and Gaussian when the SNR > 3, which is what we assume here. Using pertinent SR techniques, the high-resolution image \mathbf{x}_n can be estimated by solving the inverse problem of Equation 1:

$$\underset{\mathbf{x}_n}{\operatorname{argmin}} \sum_c \sum_j \left\| PF \{ S_{j,c} \downarrow T_j \mathbf{x}_n \} - \mathbf{y}_{j,n,c} \right\|^2 \quad (2)$$

where the choice of the least-squares criterion is motivated by the assumption that the noise is Gaussian distributed. The greater the number of acquisitions, J , with complementary information of the same object, the better the problem becomes conditioned. However, the problem in Equation 2 is often still ill-posed due to the downsampling operator, because several different intensity combinations in the high-resolution image can lead to the same intensity in the low-resolution image.

To further improve the conditioning of the problem, we can incorporate a signal model into the cost function. Given the task of T_2 quantification, it is natural to use the physical constraints imposed across the sequence of images, \mathbf{x}_n to further regularize the optimization. The signal model in its simplest form is typically described with a mono-exponential decay depending on the relaxation time map \mathbf{T}_2 and proton density map \mathbf{M}_0 :

$$\mathbf{x}_n = \mathbf{M}_0 \cdot \exp(-t_n / T_2) \quad (3)$$

where the above equation represents the pixel-wise scalar non-linear function for \mathbf{M}_0 and \mathbf{T}_2 and t_n being the TE. In this work, the first echo is ignored to alleviate the effect of stimulated echoes.²⁷ However, even with ignoring the first echo, the standard exponential fitting will result in an overestimation of \mathbf{T}_2 .⁸ A more complex model that includes effects such as \mathbf{B}_1^+ , slice profiles, multiple \mathbf{T}_2 compartments, diffusion and magnetization

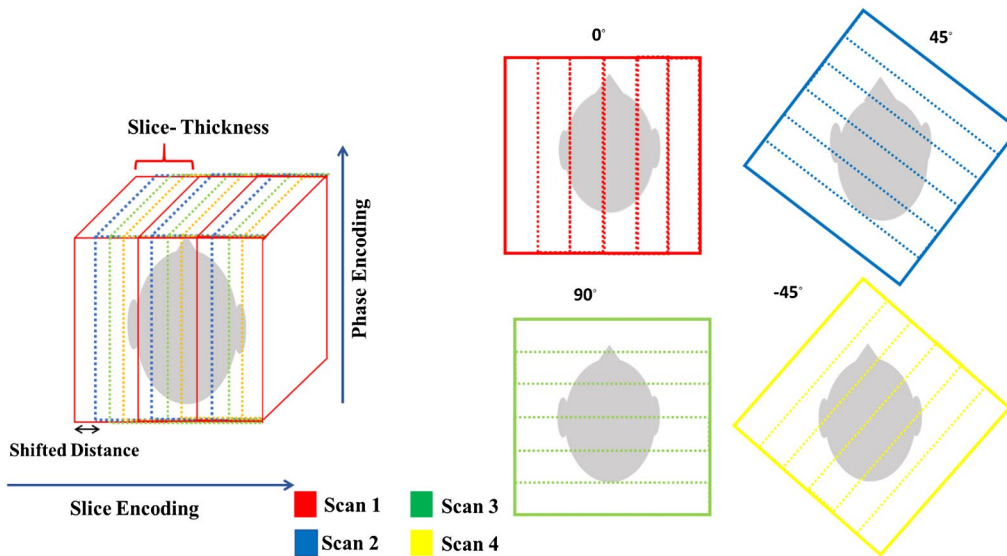


FIGURE 1 Illustration of the linear shifting (Left) and rotation (Right) experiment. The dashed lines within the boxes indicates the slice encoding direction, the frequency encoding direction is from head to toe. For the linear shifting each low-resolution scan (colors) is shifted by a known subpixel distance along the slice encoding direction (which in this case is sagittal). For illustration purposes, the shifting of the FOV (colored boxes) has been exaggerated. For rotation, each of the low-resolution scans are rotated (45°) across the common encoding direction. The red box represents sagittal section, green box represents coronal section, the blue and yellow boxes represent diagonal sections

transfer is required to accurately fit the data. Because the present work aims at a proof of concept for SR for T_2 mapping, the common approach of ignoring the first echo is used due to its simplicity and easy implementation.

In the next step of the algorithm, the most intuitive step might be to substitute the high-resolution image \mathbf{x}_n in Equation 2 with the signal-model (Equation 3) and solving directly for \mathbf{M}_0 and \mathbf{T}_2 , resulting in the following cost-function:

$$\underset{T_2, \mathbf{M}_0}{\operatorname{argmin}} \sum_j^J \sum_n^N \sum_c^C \left\| PF \{ S_{j,c} \downarrow T_j (\mathbf{M}_0 \cdot \exp(-t_n/T_2)) \} - y_{j,n,c} \right\|^2. \quad (4)$$

However, minimizing Equation 4 often requires special techniques, such as gradient scaling and repeated restarts of the optimization algorithm to achieve a fast convergence.^{7,27} Therefore, in this work, we rather formulate the minimization problem as:

$$\underset{T_2, \mathbf{M}_0, \{x_n\}_{n=1}^N}{\operatorname{argmin}} \sum_n^N \sum_c^C \sum_j^J \left\| PF \{ S_{j,c} \downarrow T_j x_n \} - y_{j,n,c} \right\|^2 + \lambda \left\| x_n - \mathbf{M}_0 \cdot \exp(-t_n/T_2) \right\|^2 \quad (5)$$

where the first term ensures data-consistency of the high-resolution image with the acquired data as in Equation 1 and an additional term ensures model-consistency, i.e., forces the signal intensities to decay exponentially across the different echoes N . In order to balance between the data- and model-consistency, a regularization parameter λ is introduced.

The above cost function in Equation 5 can be minimized using a split algorithm that estimates quantitative \mathbf{T}_2 by minimizing data- and model- consistency terms alternately.²⁰ By fixing \mathbf{T}_2 and \mathbf{M}_0 , solving Equation 5 with respect to \mathbf{x}_n amounts to a standard linear least-squares problem with a closed form solution. On the other hand, for solving Equation 5 fixing variable \mathbf{x}_n corresponds to fitting a mono-exponential decay onto \mathbf{x}_n , intrinsically estimating \mathbf{T}_2 and \mathbf{M}_0 .

3 | METHODS

3.1 | Numerical simulation

Numerical noiseless T_2 and PD maps were generated from a segmentation of gray matter (GM), white matter (WM), and cerebrospinal fluid in a single axial slice ($1 \times 1 \text{ mm}^2$ resolution) of a numerical phantom.²⁸ For the 3 main tissues, the following T_2 values were used: 0.1 s for GM, 0.06 s for WM, and 2 s for cerebrospinal fluid.²⁹ From these maps, T_2 -weighted high-resolution images \mathbf{x}_n were simulated, each with equidistant TEs ($TE = 10 \dots, 160 \text{ ms}$). The T_2 -weighted images were downsampled to the desired low-resolution using Equation 1 and different transformations

T_j . These different shifted images were then downsampled to low-resolution. Complex coil sensitivities for each of these transformations were simulated using the Parallel MRI Noisy Phantom Simulator.³⁰

These simulations exploit the fact that the reconstruction is separated into multiple 2D problems along the read-out direction (i.e., head-feet direction in this case). Therefore, for the phantom, a sagittal acquisition with phase-encoding in anterior-posterior and slice-encoding in left-right directions can be simulated. For the number of repetitions, the low-resolution single slice of the numerical phantom was shifted in the slice encoding direction (left-right). For the rotation, the FOV was rotated around the read-out (i.e., head-feet) axis for each repetition. Therefore, the applied transformations were not in-plane because the slice plane is sagittal/coronal but the numerical phantom is axial.

Three different types of transformations were tested: linear (where the images were shifted along the slice direction),²⁵ orthogonal (images were rotated to 2 orthogonal positions 0 and 90 degrees), and diagonal (2 orthogonal rotations plus 2 rotations at 45 and -45 degrees). An illustration of the different transformations is shown in Figure 1. The images were transformed to k-space and then 10-fold undersampled with a mixed parallel imaging and block undersampling pattern described in Hilbert et al.³¹ The high-resolution images were reconstructed with the proposed SR model-based reconstruction. Root mean square error (RMSE) was calculated between ground truth and reconstructed T_2 maps for all the orientations.

In principle, we assume that adding more rotations (e.g., orthogonal with 2 rotations versus diagonal with 4 rotations) will increase the accuracy of the SR reconstruction but at the expense of increased TA. To that end, various numbers of rotations (2, 4, and 5) were tested in combination with different acceleration factors (6-fold, 10-fold, 14-fold) to determine a trade-off between accuracy and TA. Approximate TAs were calculated for all the simulations with the following parameters: $1 \times 1 \text{ mm}^2$ resolution, matrix size 210×53 , and $TR = 5 \text{ s}$, 2 concatenations. The RMSE between the ground truth and the estimated T_2 map was calculated to quantify the reconstruction quality.

3.2 | Image acquisition

The proposed approach was tested on a standardized multipurpose phantom (E 38 19 195 K2130, Siemens) with 5 compartments of different concentration of $\text{MnCl}_2 \cdot 4\text{H}_2\text{O}$ in distilled water and 4 healthy subjects. Permission from the Institutional Review Board was obtained for all the in vivo imaging studies and written informed consent for the study and its publication was obtained from all participants prior to the experiments. The datasets were acquired with a standard 20-channel head/neck coil using a 10-fold undersampled

GRAPPATINI³¹ prototype sequence at 3T (MAGNETOM Skyra, Siemens Healthcare, Erlangen, Germany). The sequence implements a block undersampling pattern,⁷ which samples the k-space in blocks (or segments) that are shifted across the echoes. A classic parallel imaging scheme with 2-fold acceleration is used additionally where only every other (phase-encoding) line inside each block is acquired. For the first dataset, 50 sagittal slices with 4 mm thickness and $1 \times 1 \text{ mm}^2$ in-plane resolution were acquired. The FOV was moved by 1 mm in the slice-encoding direction with 4 shifts implementing the linear transformation. The total time of acquisition for this dataset was 16 min.

For the second dataset, 60 slices each in 2 orthogonal orientations (sagittal and coronal) and 2 diagonal orientations (sagittal > coronal 45° and -45°) with the same slice thickness and in-plane resolution were acquired. The TA for this dataset was 18 min. Additional data were acquired in the same setup (i.e., orthogonal and diagonal) with 14-fold acceleration, which reduced the TA to 11 min. Of note, the dataset with orthogonal orientation was not acquired separately, but rather the 2 diagonal orientations were removed during reconstruction to create a third dataset. Spectral fat suppression was enabled, and other relevant acquisition parameters were: TR = 5.4 s, 16 echoes, $\Delta\text{TE} = 10$ ms. For reference T_2 values, a fully sampled MESE dataset with 16 echoes and 29 slices and a resolution of $1.1 \times 1.1 \times 4 \text{ mm}^3$ was acquired. In addition, for the phantom, a conventional single-slice single-echo SE sequence with 16 TEs (10, 20, ..., 160 ms) was acquired as reference. It should be noted that the single-echo SE sequence is not a gold standard because it is still affected by diffusion, but is commonly used as a reference acquisition.^{32,33} Detailed overview of the acquisition parameters of these datasets can be found in Table 1.

3.3 | Image reconstruction

The reconstruction was implemented using Matlab (MATLAB2017a, The Mathworks Inc., Natick, MA). First, GRAPPA³⁴ was used to fill the missing lines in each block of the acquired k-space according to Hilbert et al.³¹ Using the k-space samples available at different TEs, composite fully sampled images were reconstructed and upsampled to the high-resolution grid. Subsequently, an initial guess of a T_2 and M_0 map was estimated by nonlinear least-square fitting of these magnitude high-resolution images. This estimate of the maps was then used in the algorithm for SR T_2 estimation by alternately solving Equation 5 fixing T_2 and M_0 first as described in the theory section. Complex coil sensitivities were approximated for each of the transformations by summing k-spaces across echoes. The k-space is then transformed into coil images by inverse Fourier transform and then divided by the sum of squares to obtain coil sensitivities.³⁵ The regularization parameter was heuristically set to $\lambda = 1$, establishing equal contributions from model- and

TABLE 1 Overview of the relevant protocol parameters of acquired datasets

Dataset	In-plane resolution (mm^2)	Slice thickness (mm)	Acquisition Matrix	Slices	Bandwidth (Hz)	TR (ms)	TE (ms)	No. of shifts/rotations	Acceleration Factor	No. of echoes	Scan time (mins)
Linear	1×1	4.0	240×256	50	227	4490	10	4	10	16	16
Orthogonal	1×1	4.0	240×256	60	227	5390	10	2	10	16	9
Diagonal	1×1	4.0	240×256	60	227	5390	10	4	10	16	18
Diagonal fast	1×1	4.0	224×240	56	227	4750	10	4	14	15	11
MESE- fully sampled	1.1×1.1	4.0	192×160	29	221	5000	10	-	-	16	14
SE- fully sampled	0.9×0.9	4.0	224×256	1	164	2500	10, 20, ..., 160	-	-	16	113

data-consistency in the cost function. The reconstruction was performed iteratively until no improvement was achieved in the previous 2 consecutive iterations:

$$\frac{\|X^{(i)} - X^{(i-1)}\|}{\|X^{(i)}\|} < \epsilon \quad (6)$$

where $X^{(i)}$ was the reconstructed signal series at i^{th} iteration and $\epsilon = 1e^{-04}$. In addition, the maximum number of iterations was fixed to 30 after it was experimentally tested at what iteration the algorithm typically converges (results not shown). The reconstruction scheme is illustrated in Figure 2.

3.4 | Validation

To evaluate the performance of the proposed SR model-based method, T_2 maps were qualitatively compared to T_2 maps from 2 other methods using the numerical phantom and 1 in vivo dataset. The 2 approaches were as follows:

- Low-resolution model-based + SR reconstruction: It is pertinent to assess whether minimizing the cost function jointly contributes to the better reconstruction. For this purpose, both the data consistency and model consistency were enforced 1 after the other rather in a joint cost function. First, low-resolution T_2 maps were reconstructed from individual low-resolution orientations using model-based

reconstruction, followed by a SR algorithm to upsample to a high-resolution T_2 map.

- SR reconstruction only: As described in the theory section, the signal model is used as a regularizer to better condition the minimization problem. To assess the significance of the signal model, the cost function was minimized without the model consistency term, which is equivalent to classical SR approach.

To ascertain the accuracy of the calculated T_2 values, a region of interest (ROI) analysis was performed on the phantom and in vivo T_2 maps for both accelerated and fully sampled datasets. T_2 values from different compartments of the phantom were compared with the T_2 values obtained from the conventional nonlinear least-squares fitting of the fully sampled MESE and gold standard SE data. The same comparison was made for the healthy brain where ROIs were drawn in the frontal WM, deep GM (putamen and caudate nucleus), and corpus callosum. ROI labeling and segmentation was conducted using ITK-SNAP³⁶ (www.itksnap.org). The segmentation was performed in the native space of the fully sampled T_2w images. Subsequently, the fully sampled T_2w image was pairwise registered rigidly onto the T_2 maps of the other datasets using Elastix.³⁷ The resulting transformation was then applied to the label map of the ROIs to provide a similar segmentation among datasets. The datasets of the 4 healthy volunteers who were scanned with both a 10- and 14-fold

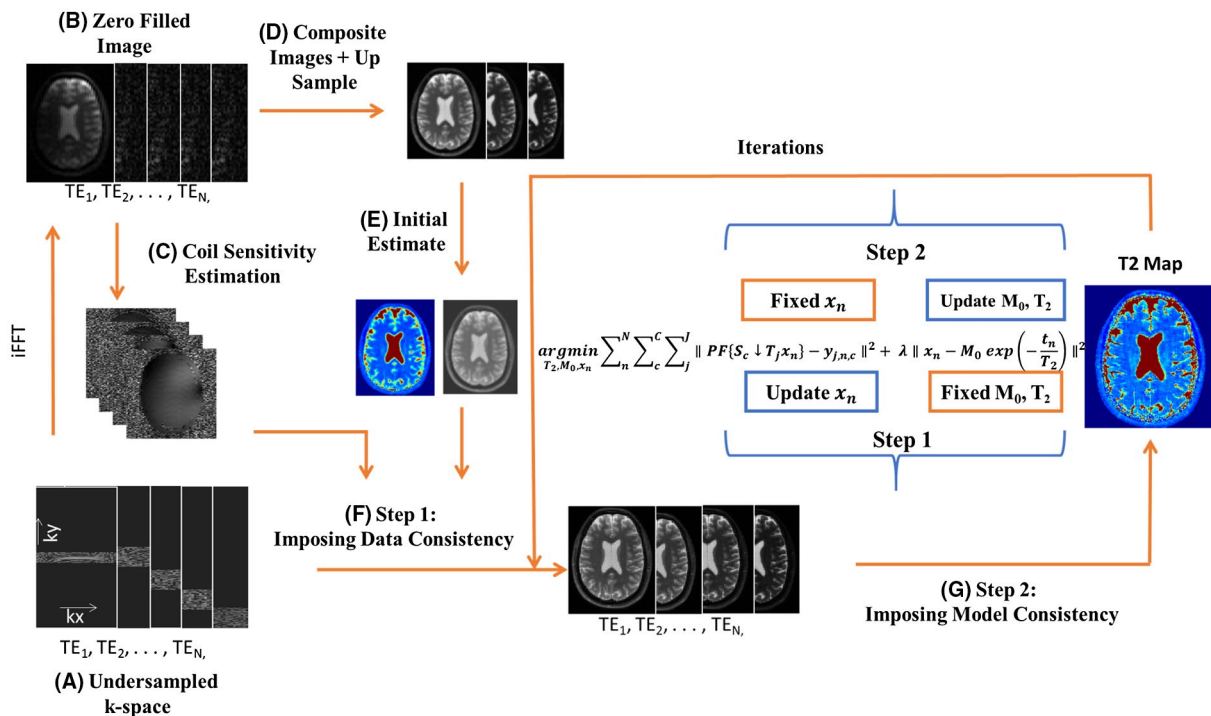


FIGURE 2 The schematic flowchart for the model-based SR reconstruction: (A) k-space data with block undersampling; (B) zero-filled image using the inverse FFT in the phase-encoding direction; (C) sensitivity maps estimation; (D) composite images are formed and upsampled to high-resolution grid; (F) data consistency is imposed as a first step of alternating minimization; (G) T_2 maps estimated by imposing model consistency in the second step. With the new estimate of T_2 , step 1 and step 2 are repeated iteratively. FFT, fast Fourier transform

accelerated acquisition with diagonal orientations and a fully sampled MESE were used in an ROI analysis as well. The T_2 values from 4 ROIs were compared across all the volunteers to ascertain the consistency of T_2 values across subjects.

4 | RESULTS

4.1 | Numerical phantom

T_2 maps and images obtained from the SR model-based reconstruction in the numerical phantom using different orientations (linear, orthogonal, and diagonal) are shown in Figure 3 in comparison to the ground truth. The diagonal rotations were better able to resolve the brain structures as compared to the linear and orthogonal datasets. This can be better appreciated in the zoomed images of the same area that demonstrates the diagonal rotation results in better delineation of the small structures in brain (Figure 3, bottom). The comparison between the 3 orientations in reconstructed T_2 -weighted images also shows sharper edges in the high-resolution images when using the diagonal orientation.

The trade-off between the number of rotations and the acceleration is demonstrated in Figure 4. The numerical simulation demonstrated that adding more rotations results in

reduced error around the edges for all the acceleration factors (from left to right). At the same time, an increased acceleration factor influences the T_2 accuracy, i.e., an increased difference from the ground truth (top to bottom). Considering the prolonged TA with the number of rotations, the best trade-off is a 10-fold accelerated scan with 4 rotations (RMSE = 7.8 ms, TA = 14 min). Five rotations and 6-fold acceleration showed the least error (RMSE = 3.2 ms) but required an TA of 29 min. The 14-fold acceleration with 5 rotations had an TA of 10 min but an RMSE of 12.5 ms. The details of the RMSE for all the accelerations and rotations are provided in Supporting Information Table S1, which is available online.

4.2 | Phantom and in vivo data

Figure 5 shows the reconstructed T_2 maps and T_2 -weighted images from 1 low-resolution acquisition, and the SR model-based reconstructed maps for linear, orthogonal, and diagonal orientations. The low-resolution T_2 maps and weighted images (Figure 5A) show partial-volume effects within the compartments of the phantom and blurring of the fine structures in the brain. Estimating T_2 maps with SR model-based reconstruction enhances the spatial resolution, reducing the partial-volume effect. However, with linear shifting, there is

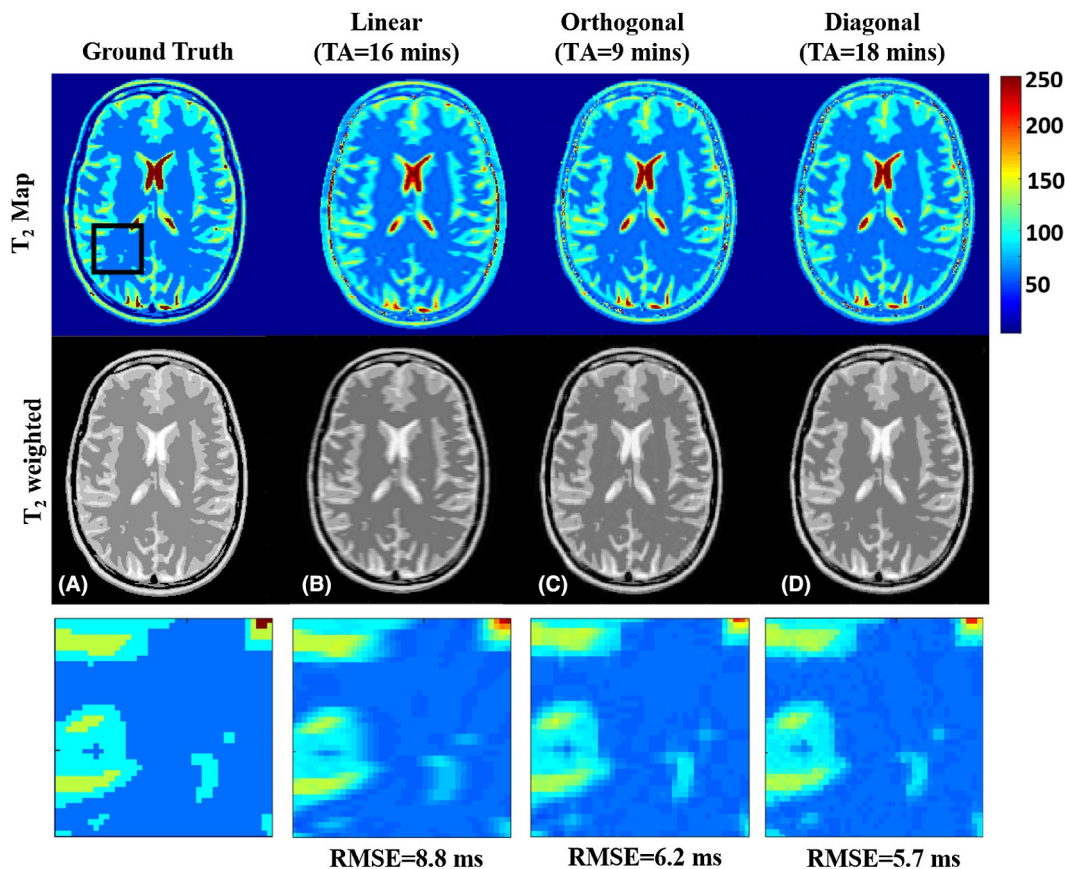


FIGURE 3 SR T_2 maps (upper row), reconstructed T_2 -weighted images (middle row), and the zoomed-in T_2 maps (bottom row) for 3 different orientations and 10-fold undersampling. A, Ground truth. B, Linear shifting. C, Orthogonal rotation. D, Diagonal rotation

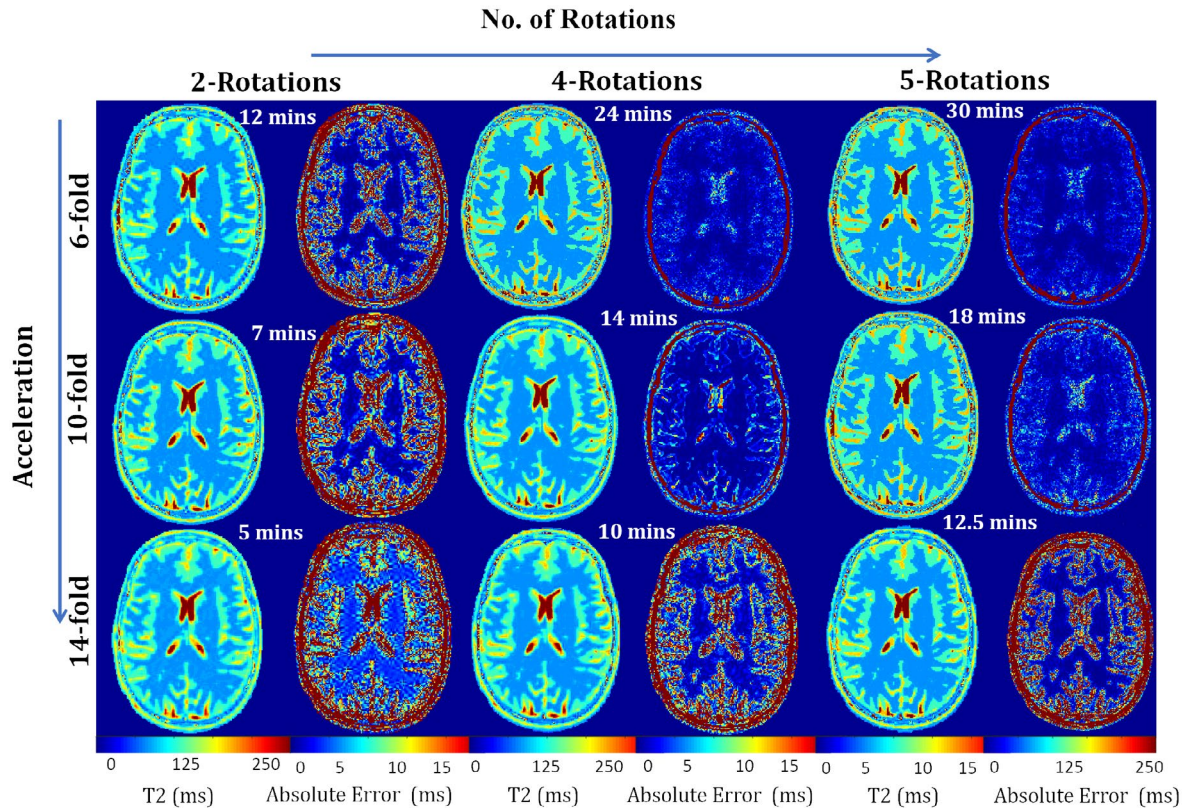


FIGURE 4 The gain in the quality of SR- T_2 reconstruction as a function of number of rotations and TA in a numerical phantom. The corresponding TAs are mentioned with the T_2 maps. Adding more rotations results in reduced error around the edges for all acceleration factors (from left to right). At the same time, the acceleration factor affects the quality of the reconstruction (top to bottom), especially for high T_2 values in the cerebral spinal fluid. Considering the increase in TA with the number of rotations, it can be deduced that the optimal configuration is 10-fold with 4 rotations

still blurring of the edges around the compartments of the phantom and brain structures (Figure 5B). For orthogonal rotations, the compartment edges in the phantoms appear sharper in both orthogonal directions (Figure 5C, white arrows), whereas the diagonal orientation improves the sharpness further, especially in the diagonal direction (Figure 5D, black arrows). The same can be observed for the human brain where diagonal rotation improved the spatial resolution and delineation of the brain structures.

Figure 6 shows the axial and coronal views of the reconstructed T_2 -weighted images from a 10-fold accelerated low-resolution dataset with diagonal orientations and the fully sampled MESE data. It is evident that the SR- T_2 mapping allows satisfactory 3D visualization due to isotropic resolution as compared to conventional MESE, which inherently has low through-plane resolution. This can be appreciated even more from the zooms shown in Figure 6. A transversal zoom on the caudate nucleus head and the putamen is shown where the interface between different structures is well delineated in both SR- T_2 -weighted and MESE- T_2 -weighted images. However, for the coronal zoom, the interface between GM and WM is better defined for SR- T_2 -weighted image.

4.3 | Validation

A comparison between the SR model-based reconstruction and the SR-only and low-resolution model-based + SR reconstruction is shown in Figure 7. For numerical phantom, nRMSEs showed that the proposed approach outperforms the SR-only and model-based + SR reconstruction. The nRMSE for SR only reconstruction was 0.50, for model-based + SR reconstruction was 0.23 and for proposed reconstruction was 0.12. The SR-only reconstruction showed visible artifacts due to the undersampling as no prior information from the signal model (mono-exponential decay) was incorporated in the reconstruction. The low-resolution model-based + SR reconstruction showed improvement in the reconstruction; however, blurring around the edges is evident in both numerical phantom and in vivo data. In comparison, SR model-based reconstruction demonstrated that combining SR and model knowledge jointly in 1 cost function improves the reconstruction.

4.4 | ROI analysis

The ROI analysis of the phantom compartments revealed that at shorter T_2 , 10-fold accelerated data were comparable

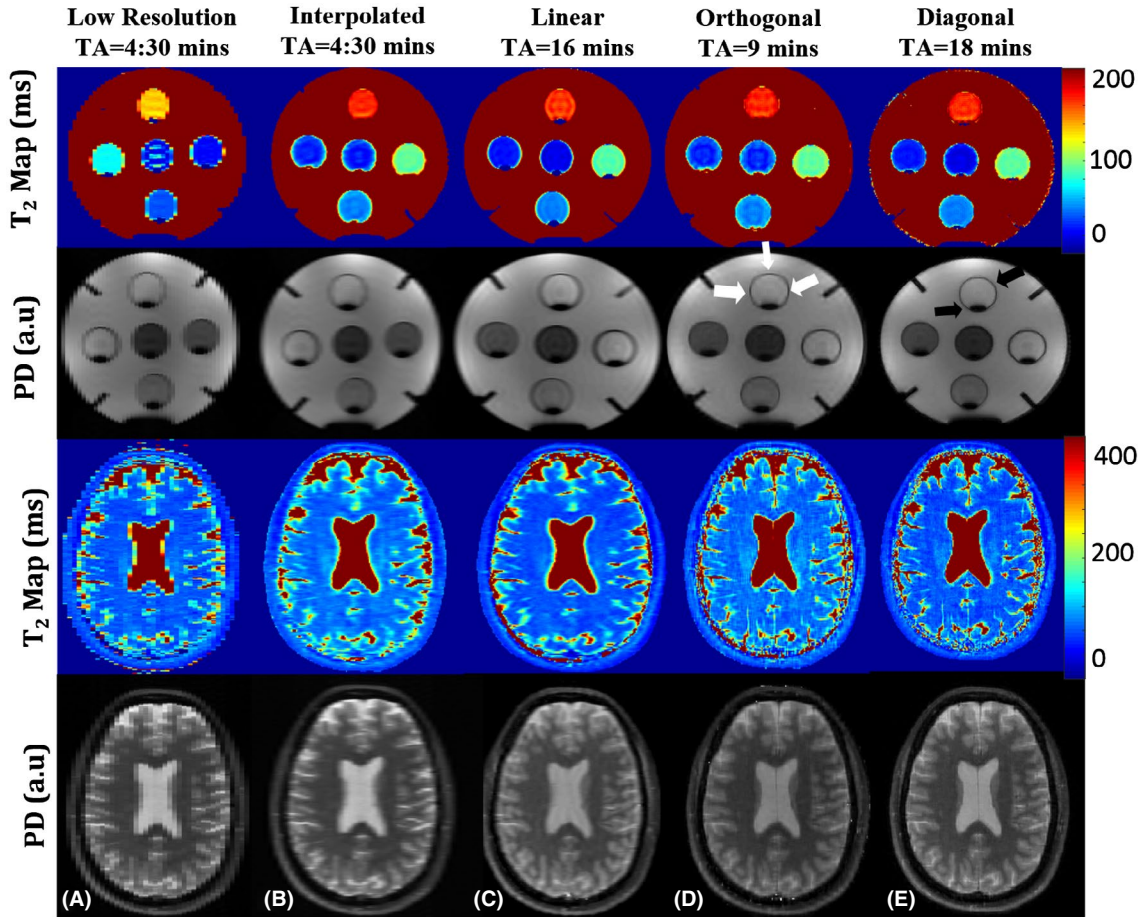


FIGURE 5 Reconstructed T_2 maps and M_0 for phantom and human brain from low-resolution (A), interpolated to high resolution grid (B), linear (C), orthogonal (D), and diagonal (E) datasets with respective TAs. For the phantom, orthogonal rotation improved the resolution as can be seen in around the edges of the compartments in 2 directions (white arrows), whereas diagonal orientation improved the resolution in 4 directions (black arrows). This can be observed in the in vivo data as well where the diagonal orientation demonstrated better resolution in brain structures as compared to orthogonal rotation and linear shift

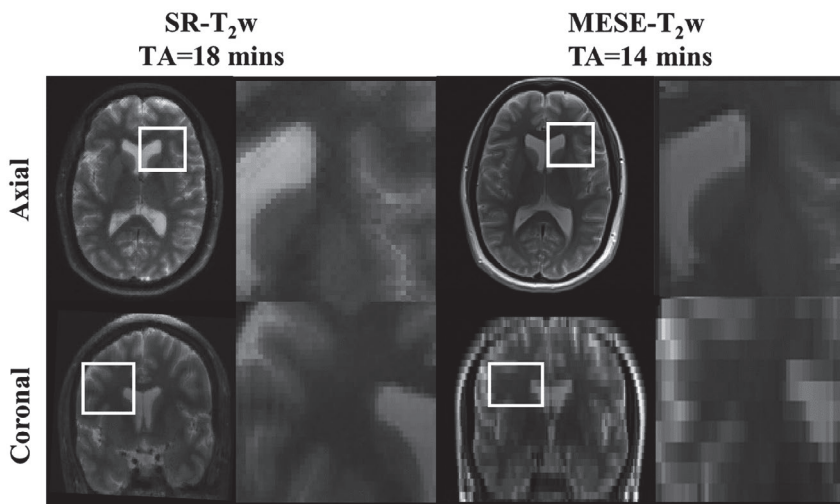


FIGURE 6 Axial and coronal views of T_2 -weighted images reconstructed with SR- T_2 mapping ($1 \times 1 \times 1 \text{ mm}^3$) (left) and T_2 -weighted image from fully sampled MESE ($1 \times 1 \times 4 \text{ mm}^3$) for $TE = 80 \text{ ms}$. The zoomed regions show the improved resolution in both planes for SR compared to the conventional sequence

with the fully sampled MESE (Figure 8A). For compartment 1, the mean T_2 value for 10-fold accelerated data was $31.1.0 \pm 1.6 \text{ ms}$, for 14-fold it was $29.25 \pm 1.7 \text{ ms}$, whereas

the T_2 value for the MESE was $25.41 \pm 1.5 \text{ ms}$ and for SE was $18.22 \pm 0.5 \text{ ms}$. For compartment 2, the mean T_2 value for 10-fold, 14-fold, MESE and the SE was $29.19 \pm 0.8 \text{ ms}$,

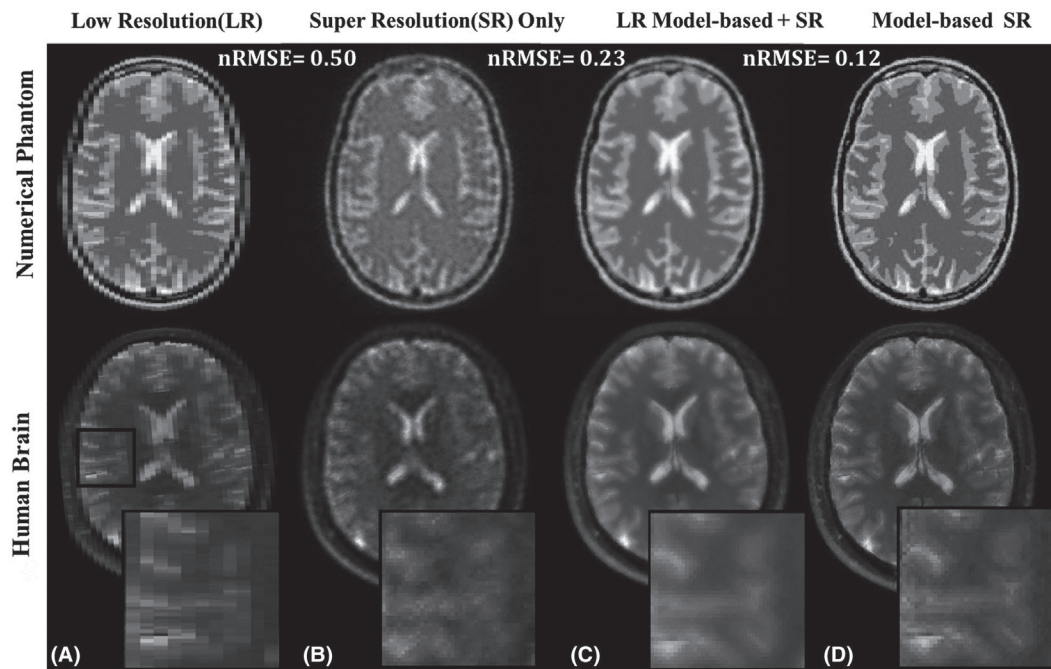


FIGURE 7 Reconstructed T_2w images ($TE = 80$ ms) from the numerical phantom and in vivo data using the diagonal orientations ($TA = 18$ min). The images are shown from a low-resolution dataset (A), SR reconstruction only (B), low-resolution model-based followed by SR reconstruction (C), and proposed SR model-based reconstruction (D). The SR only reconstruction showed visible artifacts due to the undersampling as no prior information from the signal model (mono-exponential decay) was incorporated in the reconstruction. The low-resolution model-based + SR reconstruction showed improvement in the reconstruction; however, blurring around the edges is evident in both numerical phantom and in vivo data

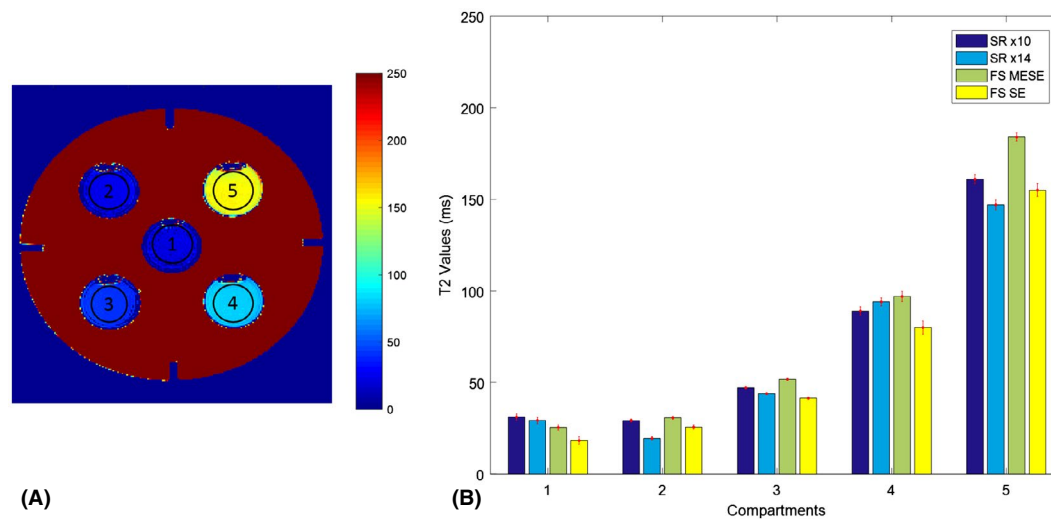


FIGURE 8 ROI Analysis for the accuracy of T_2 estimation for different dataset in different compartments of the phantom. A, T_2 map of the phantom with different compartments labels. B, The bar chart represents the mean of the T_2 values of the ROI, and the error represents the standard deviation for 10-fold, 14-fold, and fully sampled MESE and SE T_2 values

31.00 ± 0.9 ms, 30.57 ± 0.7 ms and 25.58 ± 1.1 ms, respectively. However, the error increased with higher T_2 values, with compartments 3 and 4 showing a relative difference of 10-12%. For compartment 3, the mean T_2 values for 10-fold was 47.70 ± 2 ms, for 14-fold was 43.0 ± 1.5 ms, for MESE was 51.50 ± 0.5 , and for SE was 41.0 ± 0.3 ms. The mean T_2 values for compartment 4 for 10-fold, 14-fold, MESE, and

SE were 89.00 ± 2.3 , 94.42 ± 2.1 , 96.98 ± 2.7 , and 79.96 ± 3.6 ms, respectively. For compartment 5, a greater difference ($> 15\%$) was observed with mean T_2 values of 161.7 ± 2.5 ms, 147.5 ± 2.6 ms, 184.3 ± 2.3 ms, and 155 ± 23.4 ms for 10-fold, 14-fold, MESE, and SE, respectively. All values derived with a MESE sequence were overestimated in comparison to T_2 values derived from a SE sequence. This

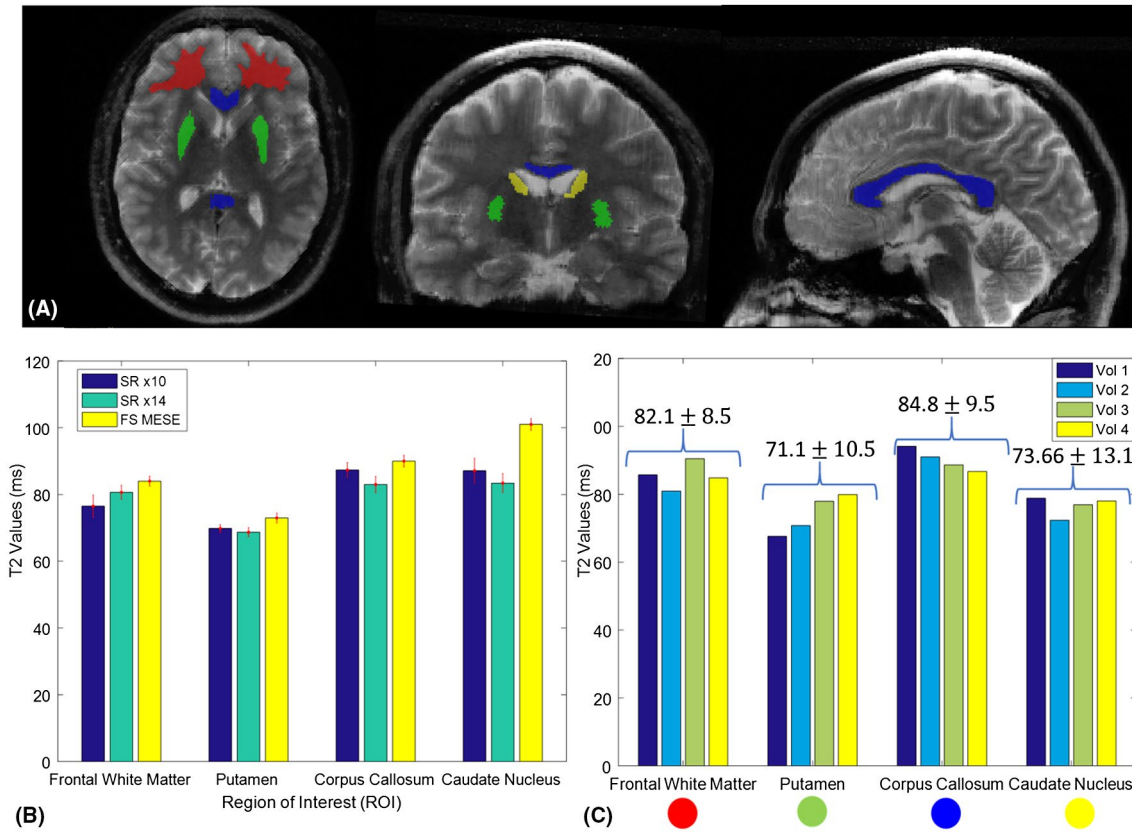


FIGURE 9 A, Different ROIs drawn in axial, coronal, and sagittal sections of a model-based SR T₂w (TE = 80 ms) image. B, The bar chart represents the mean T₂ values and standard deviation for accelerated and fully sampled dataset in 4 different regions of brain. C, The mean and standard deviation T₂ values from model-based SR reconstruction (diagonal orientations, 10-fold acceleration) found in all subjects grouped by brain structures, each bar representing a subject

overestimation is well known and caused by the stimulated echoes formed in the MESE sequence.⁶

For the in vivo data, the T₂ values in different regions of the brain showed good agreement with the fully sampled MESE acquisition (Figure 9B). For frontal WM, the mean T₂ value for the 10-fold acceleration was 80.0 ± 1.3 ms, for 14-fold it was 76.5 ± 5.1, and for MESE fully sampled it was 83.0 ± 2.1 ms. For putamen, the mean T₂ value for 10-fold, 14-fold, and MESE fully sampled was 69.8 ± 1.2, 66.2 ± 1.3, and 73.0 ± 3.1 ms, respectively. In the corpus callosum (MESE T₂ = 94 ± 2 ms), the 14-fold acceleration showed increased difference (80 ± 2.4 ms) as compared to 10-fold (87 ± 1.8 ms). The T₂ value for the caudate nucleus with the 10-fold acceleration (74.8 ± 2.0 ms) was closest to the MESE acquisition (75 ± 1.8), whereas the T₂ at 14-fold acceleration was 67 ± 2.8 ms. Comparing the mean T₂ values for 10-fold accelerated data from all the 4 ROIs across volunteers demonstrated consistent values with some natural variation (Figure 9C). The average T₂ value across all volunteers were 70.8 ± 8.5 ms for the frontal WM, 81.3 ± 10.5 ms for the putamen, 79.8 ± 9.5 ms for the corpus callosum, and 79.66 ± 13.6 ms for the caudate nucleus.

5 | DISCUSSION

The proposed work aims to address the challenges associated with high-resolution T₂ mapping with the widely used MESE sequence. The method combines SR and model-based reconstruction for T₂ estimation into 1 integrated approach, enabling the direct estimation of an isotropic high-resolution T₂ map from a set of anisotropic, undersampled, low-resolution k-spaces.

Numerical simulations demonstrated that rotating the slice orientations around the phase-encoding results in better image quality of the SR reconstruction than linear sub-pixel shifts in the slice-encoding direction. These results were confirmed by the phantom and the in vivo acquisitions where the rotation resulted in much sharper images. Low-resolution images with different slice orientations appear to better sample different spatial information than shifting the low-resolution images by subpixel distances along the slice selection direction.⁹ This is because acquiring low-frequency information in the slice-selective direction limits the additional information available in the subpixel shift. In contrast, the different orientations populate the 3D k-space much better (similar

to PROPELLER³⁸ sequences). The optimal number of slice orientations ensures that the low-resolution images contain enough spatial information to reconstruct the high-resolution image without extensively prolonging the TA. The comparison between number of rotations and acceleration factors showed that 4 slice orientations (0° , 90° , 45° , -45°) with a 10-fold acceleration was the optimum in this application with an TA of 18 min.

The advantage of combining SR with model-based reconstruction has already been demonstrated for T_1 mapping.²⁴ This work was performed in the image domain without k-space undersampling, whereas the proposed approach addresses a more complex problem by reconstructing quantitative maps from undersampled k-space data. It is important to ascertain whether model-based SR- T_2 mapping performs better than the sequential application of model-based and SR reconstructions. The comparison of the proposed approach to the SR reconstruction without prior model and to the low-resolution model-based reconstruction followed by SR reconstruction demonstrated that incorporating the model information in the reconstruction yields improved results.

Comparing a T_2 map estimated with model-based SR to a T_2 map estimated with a conventional nonlinear least-square fitting on a fully sampled MESE dataset proved that T_2 values are comparable between the 2 methods. For the phantom, the compartments with longer T_2 had a higher bias as compared to shorter T_2 compartments, which may be attributed to an imperfect signal model. One contributing factor, as already reported in the literature,⁶ is that the T_2 values derived from MESE-type acquisitions are overestimated in comparison to single-echo SE acquisitions due to stimulated-echo signal contributions, which mostly stem from an imperfect slice profile of the refocusing pulses. This can be addressed by using a different signal model which accounts for slice profile shape and B1 inhomogeneity, e.g., by using an analytical^{6,27} or numerical^{33,39,40} signal model. The current model of the proposed method does not account for the slice profile. It is assumed that incorporating it in the reconstruction will not only allow addressing stimulated-echo issues but also lead to a more realistic downsampling/upsampling operator between high-resolution and low-resolution images. Because this more accurate model will potentially further improve the spatial resolution, the slice profile is subject of future investigation.

An alternative formulation of the reconstruction problem proposed here can be as follows: the signal in a low-resolution voxel may consist of different tissue types, e.g. at a WM/GM boundary. Neglecting microstructural T_2 components, this partial volume effect yields a multi-exponential signal decay. The fitting of a mono-exponential decay in a high-resolution voxel corresponds to a multi-exponential fitting in the low-resolution image space due to the downsampling operator.

The resulting ill-posed problem becomes better conditioned because the different orientations provide selective high-resolution information, which allows us to separate out the multi-exponential components within a voxel.

Currently, the optimal-quality 10-fold accelerated acquisition lasts 18 min. Despite the high acceleration, the TA is too long to be acceptable for clinical routine or clinical studies. A higher acceleration factor (14-fold) was tested which reduced the TA to 11 min but decreased the sharpness of brain structures. Nevertheless, this long TA is still too long for clinical applications where a typical sequence requires 3 min. Various other techniques can be applied to further accelerate the TA, such as simultaneous multi-slice.^{41,42} Moreover, the same sampling pattern was used in each slice and orientation. Varying the sampling across slices and orientations may improve the reconstructed T_2 maps and will be further investigated.

SR approaches require several acquisitions with different orientations, and the reconstruction method assumes that each voxel corresponds to the same anatomical location in all the orientations. Subject motion and image distortions (e.g. due to imperfect gradient performance) violate this assumption and may not perfectly align the multiple orientations for model fitting. This model violation will lead to image artifacts and wrong T_2 values which is a limitation of the proposed method. In the frame of this study, motion correction schemes were not explored, but could be used to facilitate a better alignment of different orientations and improve the reconstruction. The area of motion correction and compensation has been well studied specifically for SR reconstruction in fetal imaging.^{43,44} Future work will aim to incorporate these strategies to further improve the robustness of the SR- T_2 mapping. In addition, incorporating a spatial regularization of the T_2 maps will potentially further improve the reconstruction.

6 | CONCLUSIONS

We propose a technique that uses four 10-fold undersampled low-resolution MESE 2D acquisitions to iteratively reconstruct a high-resolution T_2 map. The proposed technique enables high-resolution 1 mm^3 isotropic whole-brain T_2 mapping in 18 min. The proposed technique may allow the assessment of T_2 values in small brain structures valuable for the search of imaging biomarkers in the future.

ORCID

Wajiha Bano  <https://orcid.org/0000-0002-0602-5116>

Gian Franco Piredda  <https://orcid.org/0000-0002-8449-6634>

Tom Hilbert  <https://orcid.org/0000-0001-8207-4908>

REFERENCES

1. Siemonsen S, Mouridsen K, Holst B, et al. Quantitative t2 values predict time from symptom onset in acute stroke patients. *Stroke*. 2009;40:1612–1616.
2. Cheng HL, Stikov N, Ghugre NR, Wright GA. Practical medical applications of quantitative MR relaxometry. *J Magn Reson Imaging*. 2012;36:805–824.
3. Bonnier G, Roche A, Romascano D, et al. Advanced MRI unravels the nature of tissue alterations in early multiple sclerosis. *Ann Clin Transl Neurol*. 2014;1:423–432.
4. Blystad I, Warntjes JM, Smedby Ö, Lundberg P, Larsson E-M, Tisell A. Quantitative MRI for analysis of peritumoral edema in malignant gliomas. *PLoS ONE*. 2017;12:e0177135.
5. Carr HY, Purcell EM. Effects of diffusion on free precession in nuclear magnetic resonance experiments. *Phys Rev*. 1954;94:630.
6. Petrovic A, Scheurer E, Stollberger R. Closed-form solution for T2 mapping with nonideal refocusing of slice selective CPMG sequences. *Magn Reson Med*. 2015;73:818–827.
7. Sumpf TJ, Uecker M, Boretius S, Frahm J. Model-based nonlinear inverse reconstruction for T2 mapping using highly undersampled spin-echo MRI. *J Magn Reson Imaging*. 2011;34:420–428.
8. McPhee KC, Wilman AH. Limitations of skipping echoes for exponential T2 fitting. *J Magn Reson Imaging*. 2018;48:1432–1440.
9. Plenge E, Poot DHJ, Bernsen M, et al. Super-resolution methods in MRI: can they improve the trade-off between resolution, signal-to-noise ratio, and acquisition time? *Magn Reson Med*. 2012;68:1983–1993.
10. Greenspan H, Oz G, Kiryati N, Peled S. MRI inter-slice reconstruction using super-resolution. *Magn Reson Imaging*. 2002;20:437–446.
11. Hennig J. Multiecho imaging sequences with low refocusing flip angles. *J Magn Reson (1969)*. 1988;78:397–407.
12. Block KT, Uecker M, Frahm J. Model-based iterative reconstruction for radial fast spin-echo MRI. *IEEE Trans Med Imaging*. 2009;28:1759–1769.
13. Doneva M, Börnert P, Eggers H, Stehning C, SÉNÉgas J, Mertins A. Compressed sensing reconstruction for magnetic resonance parameter mapping. *Magn Reson Med*. 2010;64:1114–1120.
14. Ma D, Gulani V, Seiberlich N, et al. Magnetic resonance fingerprinting. *Nature*. 2013;495:187.
15. Zhang T, Pauly JM, Levesque IR. Accelerating parameter mapping with a locally low rank constraint. *Magn Reson Med*. 2015;73:655–661.
16. Petzschner FH, Ponce IP, Blaimer M, Jakob PM, Breuer FA. Fast MR parameter mapping using k-t principal component analysis. *Magn Reson Med*. 2011;66:706–716.
17. Lustig M, Donoho D, Pauly JM. Sparse MRI: the application of compressed sensing for rapid MR imaging. *Magn Reson Med*. 2007;58:1182–1195.
18. Velikina JV, Alexander AL, Samsonov A. Accelerating MR parameter mapping using sparsity-promoting regularization in parametric dimension. *Magn Reson Med*. 2013;70:1263–1273.
19. Peled S, Yeshurun Y. Superresolution in MRI—perhaps sometimes. *Magn Reson Med*. 2002;48:409–409.
20. Carmi E, Liu S, Alon N, Fiat A, Fiat D. Resolution enhancement in MRI. *Magn Reson Imaging*. 2006;24:133–154.
21. Scheffler K. Superresolution in MRI? *Magn Reson Med*. 2002;48:408–408.
22. Scherrer B, Gholipour A, Warfield SK. Super-resolution reconstruction to increase the spatial resolution of diffusion weighted images from orthogonal anisotropic acquisitions. *Med Image Anal*. 2012;16:1465–1476.
23. Van Steenkiste G, Jeurissen B, Veraart J, et al. Super-resolution reconstruction of diffusion parameters from diffusion-weighted images with different slice orientations. *Magn Reson Med*. 2016;75:181–195.
24. Van Steenkiste G, Poot DH, Jeurissen B, et al. Super-resolution T1 estimation: quantitative high resolution T1 mapping from a set of low resolution T1-weighted images with different slice orientations. *Magn Reson Med*. 2017;77:1818–1830.
25. Hilbert T, Marques JP, Thiran J-P, Meuli R, Krueger G, Kober T. Model-based super-resolution reconstruction of T2 maps. *Proc Intl Soc Mag Reson Med*. 2017.
26. Gudbjartsson H, Patz S. The Rician distribution of noisy MRI data. *Magn Reson Med*. 1995;34:910–914.
27. Sumpf TJ, Petrovic A, Uecker M, Knoll F, Frahm J. Fast T2 mapping with improved accuracy using undersampled spin-echo MRI and model-based reconstructions with a generating function. *IEEE Trans Med Imaging*. 2014;33:2213–2222.
28. Guerquin-Kern M, Lejeune L, Pruessmann KP, Unser M. Realistic analytical phantoms for parallel magnetic resonance imaging. *IEEE Trans Med Imaging*. 2012;31:626–636.
29. McRobbie DW, Moore EA, Graves MJ. *MRI from Picture to Proton*. Cambridge: Cambridge University Press; 2017.
30. Aja-Fernández S, Tristán-Vega A. Influence of noise correlation in multiple-coil statistical models with sum of squares reconstruction. *Magn Reson Med*. 2012;67:580–585.
31. Hilbert T, Sumpf TJ, Weiland E, et al. Accelerated T2 mapping combining parallel MRI and model-based reconstruction: GRAPPATINI. *J Magn Reson Imaging*. 2018;48:359–368.
32. Huang C, Bilgin A, Barr T, Altbach MI. T2 relaxometry with indirect echo compensation from highly undersampled data. *Magn Reson Med*. 2013;70:1026–1037.
33. Ben-Eliezer N, Sodickson DK, Block KT. Rapid and accurate T2 mapping from multi-spin-echo data using Bloch-simulation-based reconstruction. *Magn Reson Med*. 2015;73:809–817.
34. Griswold MA, Jakob PM, Heidemann RM, et al. Generalized auto-calibrating partially parallel acquisitions (GRAPPA). *Magn Reson Med*. 2002;47:1202–1210.
35. Pruessmann KP, Weiger M, Scheidegger MB, Boesiger P. SENSE: sensitivity encoding for fast MRI. *Magn Reson Med*. 1999;42:952–962.
36. Yushkevich PA, Piven J, Hazlett HC, et al. User-guided 3D active contour segmentation of anatomical structures: significantly improved efficiency and reliability. *NeuroImage*. 2006;31:1116–1128.
37. Klein S, Staring M, Murphy K, Viergever MA, Pluim JP. Elastix: a toolbox for intensity-based medical image registration. *IEEE Trans Med Imaging*. 2010;29:196–205.
38. Pipe JG. Motion correction with PROPELLER MRI: application to head motion and free-breathing cardiac imaging. *Magn Reson Med*. 1999;42:963–969.
39. Ben-Eliezer N, Sodickson DK, Shepherd T, Wiggins GC, Block KT. Accelerated and motion-robust in vivo T2 mapping from radially undersampled data using bloch-simulation-based iterative reconstruction. *Magn Reson Med*. 2016;75:1346–1354.

40. Neumann D, Blaimer M, Jakob PM, Breuer FA. Simple recipe for accurate T₂ quantification with multi spin-echo acquisitions. *MAGMA*. 2014;27:567–577.
41. Barth M, Breuer F, Koopmans PJ, Norris DG, Poser BA. Simultaneous multislice (SMS) imaging techniques. *Magn Reson Med*. 2016;75:63–81.
42. Hilbert T, Schulz J, Marques JP, et al. Fast model-based T₂ mapping using SAR-reduced simultaneous multislice excitation. *Magn Reson Med*. 2019:1–14.
43. Pier DB, Gholipour A, Afacan O, et al. 3D Super-resolution motion-corrected MRI: validation of fetal posterior fossa measurements. *J Neuroimaging*. 2016;26:539–544.
44. Tourbier S, Bresson X, Hagmann P, Thiran J-P, Meuli R, Cuadra MB. An efficient total variation algorithm for super-resolution in fetal brain MRI with adaptive regularization. *NeuroImage*. 2015;118:584–597.

SUPPORTING INFORMATION

Additional supporting information may be found online in the Supporting Information section at the end of the article.

SUPPORTING INFORMATION TABLE S1 RMSE (ms) calculated for different rotations (right to left) and accelerations (top to bottom)

How to cite this article: Bano W, Piredda GF, Davies M, et al. Model-based super-resolution reconstruction of T₂ maps. *Magn Reson Med*. 2020;83:906–919. <https://doi.org/10.1002/mrm.27981>